Preparation, characterization and photocatalytic properties of cerium doped TiO$_2$: On the effect of Ce loading on the photocatalytic reduction of carbon dioxide

Lenka Matějová [a,*], Kamila Kočí [b], Martin Reli [b], Libor Čapek [d], Alice Hospodková [e], Pavlína Peikertová [a], Zdeněk Matěj [f], Lucie Obalová [c], Anna Wach [g], Piotr Kuśtrowski [g], Andrzej Kotarba [g]

[a] Nanotechnology Centre, VŠB-Technical University of Ostrava, 17, listopadu 15/2172, Ostrava 708 33, Czech Republic
[b] Energy Units for Utilization of non Traditional Energy Sources, VŠB-Technical University of Ostrava, 17, listopadu 15/2172, Ostrava 708 33, Czech Republic
[c] Institute of Environmental Technology, VŠB-Technical University of Ostrava, 17, listopadu 15/2172, Ostrava 708 33, Czech Republic
[d] Department of Physical Chemistry, Faculty of Chemical Technology, University of Pardubice, Studentská 573, Pardubice 532 10, Czech Republic
[e] Institute of Physics of the ASCR, v.v.i., Na Slovance 2, Prague 8 182 21, Czech Republic
[f] Department of Condensed Matter Physics, Faculty of Mathematics and Physics, Charles University in Prague, Ke Karlovu 5, Prague 2 121 16, Czech Republic
[g] Faculty of Chemistry, Jagiellonian University, Ingardena 3, Krakow 30 060, Poland

ABSTRACT

The parent TiO$_2$ and cerium doped TiO$_2$ photocatalysts with Ce loadings 0.28–10 mol.% were prepared by the sol-gel method controlled within reverse micelles of nonionic surfactant Triton X-114. Photocatalysts were comprehensively characterized using nitrogen physisorption, XRD, XPS, contact potential difference measurements, Raman spectroscopy, and DR UV–vis spectroscopy and their performance was explored in the CO$_2$ photocatalytic reduction for the first time. Concerning photocatalysts properties, it was revealed that the inhibiting effect of cerium on the TiO$_2$ crystallites growth occurred only up to 3 mol.% of Ce when the incorporation of Ce^{4+} into the anatase lattice took place. This phenomenon was correlated with the expansion of anatase cell volume. At higher Ce loadings ($\geq$5 mol.%) the anatase lattice was saturated and the formation/separation of amorphous ceria and/or ceria ($\sim$1 nm) nucleation occurred, accompanied by the increase of TiO$_2$ anatase crystallite-size and the limitation of value of anatase cell volume. Further, it was found out that the mesoporosity of photocatalysts may be preferentially attributed to voids existing between the individual crystallites and thus can be influenced by changes in the crystallite size. The modification of TiO$_2$ with cerium affected also the spectral response of photocatalysts, shifting it to the visible light region. However, this property itself was not crucial in the CO$_2$ photocatalytic reduction. The key role in the CO$_2$ photocatalytic reduction played the energies of electrons and holes within the electronic structure of photocatalysts, which were markedly affected by the Ce atoms addition. For 0.28 mol.%Ce/TiO$_2$, both electrons and holes have required potentials for the photocatalytic reduction of CO$_2$, while for 3 mol.% and higher Ce loadings the energy of electrons was already below H$^+$ reduction potential and thus the photocatalytic performance of these catalysts was decreasing.

© 2014 Elsevier B.V. All rights reserved.

1. Introduction

In recent years titania–ceria mixed oxides and cerium ions (Ce^{3+}, Ce^{4+}) doped titania have been intensively examined because of their high application potential as an electrode material in electrochromic devices [1–4], sensing film gas sensors [5,6], coatings for self-cleaning surfaces [7], or in heterogeneous catalysis as a noble metal catalysts support [8,9] or photocatalysts [10–20]. A lot of efforts have been devoted to their investigation in photodegradation of various organic toxic pollutants in liquid phase such as dyes [16–18], pesticides [14,19] or 4-chlorophenol [20]. The enhanced photocatalytic performance of both, cerium ions doped titania as well as some titania–ceria mixed oxides, was proved. However, it should be noted that the cerium doped titania photocatalysts must be tailored with respect to degraded compounds.

Much less attention has been focused on the photocatalytic degradation of gaseous pollutants, e.g. CO$_2$, N$_2$O, contributing to global warming. It can be said that the increasing concentration of atmospheric carbon dioxide in a consequence of fossil fuel burning

* Corresponding author. Tel.: +420 597 327 310.
E-mail address: lenka.matejova@vsb.cz (L. Matějová).

has been considered as a serious environmental problem [21,22] which should be solved. All up-to-date published papers focused on the photocatalytic reduction of CO_2 over variously doped TiO_2 were profusely reported in the review from Liu et al. [23].

On the other hand, only one paper concerning Ce-modified TiO_2 photocatalysts for the CO_2 photocatalytic reduction has been reported recently by Wang et al. [24]. They studied ordered mesoporous CeO_2–TiO_2 composites (33–66 mol.% CeO_2) with 2D hexagonal structure, synthesized through a nanocasting route using ordered mesoporous SBA-15 as the template, titanium tetrachloride and cerium nitrate as the Ti and Ce oxide phase precursors. The main products of the CO_2 reduction with water vapor under simulated solar irradiation were CO and CH_4. Besides that, they found out the following features; (i) the ordered mesoporous architecture of CeO_2–TiO_2 composites with large surface area (140–182 m^2/g) and 2D open pore system makes facile the reactant diffusion into the bulk of catalyst and hence provides fast intraparticle molecular transfer, (ii) the introduction of CeO_2 species into composites can effectively extend the spectral response from UV to visible area, (iii) the CeO_2 addition can enhance the amount of surface chemisorbed oxygen species on the ordered mesoporous CeO_2–TiO_2 composites, these oxygen species can easily capture electrons and yield surface oxygen radicals with excellent reduction capability, (iv) the existence of mixture of Ce^{3+}/Ce^{4+} oxidation states on the surface of CeO_2–TiO_2 composites denotes that the metal cations in the composites are not fully oxidized, so that Ce^{3+} can interact with holes and prevent the combination of photogenerated electrons and holes, resulting in a higher quantum efficiency of photocatalytic reaction and finally (v) the CeO_2–TiO_2 composites show good structural stability. Thus, the excellent photocatalytic activity of CeO_2–TiO_2 composites in the CO_2 photocatalytic reduction was attributed to their peculiar composition and structural characteristics.

Based on the fact that the performance of TiO_2 catalysts doped with low cerium loadings has not been investigated in the photocatalytic CO_2 reduction yet, and several above mentioned papers indicate possible functionality of this type of photocatalysts in this reaction, this paper reports on the synthesis, characterization and examination of a set of nanoparticulated cerium doped TiO_2 (with 0–10 mol.% of Ce) in the CO_2 photocatalytic reduction, for the first time.

Cerium doped TiO_2 photocatalysts are synthesized using the sol-gel process controlled within reverse micelles of non-ionic surfactant Triton X-114 in cyclohexane, using titanium(IV) isopropoxide and cerium(III) nitrate hexahydrate as metal oxide precursors. Physicochemical, optical and electronic properties of photocatalysts are characterized using nitrogen physisorption, powder X-ray diffraction (XRD), Raman spectroscopy, X-ray photoelectron spectroscopy (XPS), UV–vis diffuse reflectance spectroscopy and the contact potential difference (V_{CPD}) measurements. The determined properties of photocatalysts are correlated with their performance in the photocatalytic CO_2 reduction.

2. Experimental

2.1. Preparation of cerium doped TiO_2 photocatalysts

The parent TiO_2 and a set of cerium doped TiO_2 photocatalysts (with 0.28, 3, 5, and 10 mol.% of Ce) were prepared via sol–gel processing controlled within reverse micelles of nonionic surfactant Triton X-114 in cyclohexane in combination with calcination [25,26]. Titanium(IV) isopropoxide ($Ti(OCH(CH_3)_2)_4$, purity >97%, Aldrich) and cerium(III) nitrate hexahydrate ($Ce(NO_3)_3·6H_2O$, Aldrich) were used as metal cations sources. For TiO_2 synthesis the molar ratio of cyclohexane: Triton X-114: H_2O: $Ti(OCH(CH_3)_2)_4$ was

kept 11: 1: 1: 1 [25]. For Ce-doped TiO_2 synthesis the molar ratio of cyclohexane: Triton X-114: H_2O: $Ce(NO_3)_3·6H_2O + Ti(OCH(CH_3)_2)_4$ was kept 16.5: 3: 3: 1 [26], changing the Ce:Ti molar ratio particularly. The prepared sols were poured in a thin layer on Petri's dishes and left for 48 h on air at ambient temperature and pressure for gelation. The sols converted into rigid transparent yellow-colored gels. The titania and cerium doped titania gels were thermally treated at 350 °C for 4 h and then up to 500 °C for 2 h with heating rate 1 °C/min in order to produce powder photocatalysts. All prepared solids were sieved to particle size <0.160 mm.

2.2. Characterization of photocatalysts

Nitrogen physisorption was performed on the automated volumetric apparatus Sorptomatic 1990 (Thermo Fisher Scientific Inc.) after sample degassing at 105 °C for 5 h under less than 1 Pa vacuum. The adsorption–desorption isotherms of nitrogen were measured at −196 °C. The specific surface area, S_{BET}, was calculated according to the classical Brunauer–Emmett–Teller (BET) theory for the p/p_0 range = 0.05–0.25 [27,28]. The micropore volume, V_{micro}, and the mesopore surface area, S_{meso}, were evaluated by t-plot method [29] using Lecloux–Pirard standard isotherm with C constant [30–32]. The total pore volume, V_{total}, was determined from nitrogen adsorption isotherm at p/p_0 of 0.995. Pore size distribution (PSD) was evaluated from the desorption branch of the nitrogen adsorption-desorption isotherm using BJH method [33,34], the empirical Lecloux–Pirard standard isotherm and assuming the cylindrical pore geometry.

The XRD patterns were measured using a Bruker D8 Advance 90 diffractometer in the Bragg–Brentano geometry, equipped with a VANTEC 1 fast position sensitive detector and using Ni-filtered CoKα radiation (λ = 1.789 Å). Measurements were carried out in the reflection mode, powder samples were pressed in a rotational holder. The NIST lanthanum 92 hexaboride (LaB_6) line profile standard was measured in the same experimental arrangement as investigated samples to characterize instrumental effects. The crystallite size and the lattice parameters were evaluated from Rietveld refinement of XRD data using computer program MStruct [35,36]. The method and the model were described in more detail in Ref. [35,37].

Raman spectra were collected on a Smart System XploRA^{TM} (Horiba Jobin Yvon, France) using 532 nm laser source. An Olympus microscope BX 41/51 with an objective magnification of 50 was used to focus the laser beam on the sample placed on an X–Y motorized sample stage. Filter was used to reduce laser beam to 1% of initial intensity and grating 1200 gr./mm was used. The band widths at half maximum (FWHM) were determined by spectral deconvolution after normalizing the spectral band. The present FWHMs were evaluated from the set of ten Raman spectra acquired from ten different places within each sample.

XPS spectra were recorded on a Prevac photoelectron spectrometer equipped with a hemispherical VG SCIENTA R3000 analyzer. The photoelectron spectra were measured using a monochromatized aluminum AlKα source (E = 1486.6 eV) and a low energy electron flood gun (FS40A-PS) to compensate the charge on the surface of nonconductive samples. The base pressure in the analysis chamber during the measurements was $5 × 10^{-9}$ mbar. Spectra were recorded with constant pass energy of 100 eV for the survey and for high resolution spectra. The binding energies were referenced to C1s core level (E_b = 284.6 eV). The composition and chemical surrounding of the sample surface were investigated on the basis of the areas and binding energies of Ce 3d, Ti 2p, O 1s and C 1s photoelectron peaks. The fitting of high resolution spectra was provided through the CasaXPS software.

UV–vis diffuse reflectance spectra of prepared samples (grain size <0.160 mm) were measured by using a GBS CINTRA 303
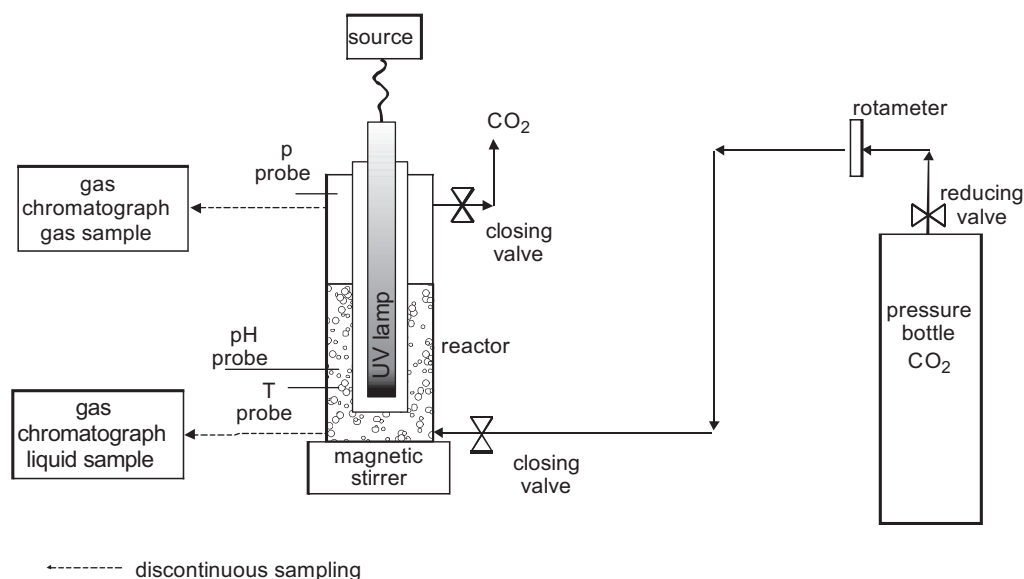
Fig. 1. The block scheme of the set-up for photocatalytic CO_2 reduction.

spectrometer equipped with a Spectralon-coated integrating sphere using a Spectralon coated discs as a standard. The spectra were recorded in the range of the wavelength 200–800 nm (lamps switched at 350 nm). The reflectances were re-calculated to the absorption using the Schuster–Kubelka–Munk equation, $F(R_\infty) = (1 - R_\infty)^2/2R_\infty$, where R_∞ is the diffuse reflectance from a semi-infinite layer. The obtained spectra were transformed to the dependencies $(F(R_\infty) \times h\nu)^2$ against $h\nu$ and assuming that the Tauc's law [38] can be expressed as: $(F(R_\infty) \times h\nu)^2 \approx (h\nu - \varepsilon_0)$, where the ε_0 – the energy of absorption edge values (determined from obtained plots), h – Planck constant and ν – frequency. Kubelka–Munk function was used to estimate the band gap energy of the prepared photocatalysts. The optical absorption threshold (lg) was calculated using the equation, $lg = 1240/EB$, where EB is the band gap energy.

The contact potential difference (V_{CPD}) measurements were carried out by the dynamic condenser method of Kelvin with a KP6500 probe (McAllister Technical Services). The reference electrode was a standard stainless steel plate with diameter of 3 mm ($\Phi_{ref} = 4.3$ eV) provided by the manufacturer. During the measurements the gradient of the peak-to-peak versus backing potential was set to 0.2, whereas the vibration frequency and amplitude was set to 120 Hz and 40 a.u. The final V_{CPD} value was an average of 60 independent points using two backing potentials. The measurements were carried out under atmospheric pressure and ambient temperature. Before the measurements the samples were pressed into pellets of 10 mm diameter using the 8 MPa pressure. The work function values were obtained from a simple relation $V_{CPD} = \Phi_{ref} - \Phi_{sample}$.

2.3. Photocatalytic tests

The photocatalytic reduction of carbon dioxide was carried out in a stirred batch annular reactor with a suspended catalyst illuminated by UV 8 W Hg lamp with a peak light intensity at 254 nm (Ultra-Violet Products Inc., USA, 11SC-1) situated in the centre of the quartz tube; the shell tube was made from stainless steel (Fig. 1). A supercritical fluid-grade CO_2 with a certified maximum of hydrocarbons less than 1 ppm was used as the reactant (SIAD Technical Gases, CZ) to avoid any hydrocarbon contamination from reaction gas. The 0.2 mol/l NaOH was used as a reduction medium. GC/FID/TCD was used for the analysis of gaseous reaction products.

The details about the CO_2 photocatalytic reduction experiment and analytical methods were described in our previous publication [39].

It was important to minimize the influence of transport phenomena during kinetic measurements. Thus, the catalyst loading of 1 g·dm^{-3} was chosen to avoid concentration gradients in the bulk of stirred liquid with suspended catalyst due to the scattering effect of light caused by the high solid concentration [40,41]. The determination of suitable volume of the liquid phase in the annular photo-reactor to fulfill the requirement of perfect mixing has been found to be 100 ml [42].

All data were measured twice. The accuracy of measurements was verified by series of repeated measurements and the relative error of products yields (μmol·g^{-1}) of 10% was determined.

Blank reactions were also performed to ensure that the hydrocarbon production was due to the photoreduction of CO_2 and to eliminate the surrounding interference. The first blank was UV-illuminated catalyst in the absence of CO_2 and the second blank was in the dark with the catalyst and CO_2 under the same experimental conditions. No CH_4, CO and H_2 were detected in the above blank tests.

3. Results and discussion

3.1. Photocatalysts characterization

The synthesized catalysts were characterized using several complementary investigation techniques in order to determine their physicochemical, optical and electronic properties which could contribute to explain their performance in the photocatalytic CO_2 reduction.

Surface area and porous structure morphology

The evaluated textural properties of all investigated photocatalysts are summarized in Table 1 and the measured nitrogen adsorption-desorption isotherms and the evaluated pore-size distributions are shown in Fig. 2a and b, respectively. It can be seen from Fig. 2a that all tested photocatalysts possess the nitrogen adsorption–desorption isotherm corresponding to the combination of IV and I isotherm types according to IUPAC classification, typical for mesoporous material having more or less amounts of micropores. This joint feature agrees with evaluated textural properties of

Table 1
Textural and optical properties of investigated photocatalysts.

Photocatalyst	Nitrogen physisorption				UV–Vis
	S_{BET} (m²/g)	S_{meso} (m²/g)	V_{micro} (mm³$_{liq}$/g)	V_{net} (mm³$_{liq}$/g)	Absorption edge (eV)
TiO$_2$	37	24	8	99	3.19
0.28 mol.%Ce/TiO$_2$	81	56	16	159	3.08
3 mol.%Ce/TiO$_2$	122	80	27	294	2.72
5 mol.%Ce/TiO$_2$	113	76	25	241	2.74
10 mol.%Ce/TiO$_2$	98	66	21	171	2.64

photocatalysts summarized in Table 1. As the specific surface area, S_{BET}, is not a trustworthy parameter in the case of analysis of microporous - mesoporous solids because of incorrect application of the classic (two-parameter) BET theory designed for purely mesoporous or nonporous solids for the analysis of adsorption isotherms [27,28], the mesopore surface area, S_{meso}, and the micropore volume, V_{micro}, were also evaluated using the t-plot method. Pure TiO$_2$, of which the isotherm corresponds to the lowest adsorbed amount of nitrogen (~99 mm³$_{liq}$/g), possesses the lowest mesopore surface area (~24 m²/g) with small amount of micropores. With increasing amount of loaded cerium to 3 mol.% the net pore volume as well as the mesopore surface area of photocatalysts significantly increased to 294 mm³$_{liq}$/g and 80 m²/g, respectively. The further increase of cerium amount loaded in TiO$_2$ up to 10 mol.% led surprisingly to the decrease of photocatalysts' net pore volume as well as the mesopore surface area to 171 mm³$_{liq}$/g and 66 m²/g, respectively. Concerning the change of the ratio of micropore volume to net pore volume in all investigated photocatalysts, with increasing amount of cerium it stayed practically constant within 8–12%. Thus, it is evident that the cerium amount influences significantly the surface area of photocatalysts, which can be related to some structural changes caused by the presence of cerium. Hence, in the following part the comprehensive attention was focused on the revealing of structural and surface properties of investigated photocatalysts and their mutual correlation.

Structural properties and the correlation between XRD and nitrogen physisorption results

Structural properties as the crystallinity, the phase composition and the crystallite-size of investigated photocatalysts were examined using powder X-ray diffraction. The XRD patterns of all examined photocatalysts are shown in Fig. 3a. Parent TiO$_2$ as well as all cerium doped TiO$_2$ show the diffraction lines corresponding only to TiO$_2$ anatase $h\,k\,l$ reflections. However, in parent TiO$_2$ besides the main anatase (1 0 1), (0 0 4) and (2 0 0) $h\,k\,l$ reflections at 29.4°,

Table 2
Structural properties of investigated photocatalysts determined by using XRD.

Photocatalyst	$<D>_V$ [a] (nm)	Unit cell parameters		
		a (Å)	c (Å)	V_{cell} (Å³)
TiO$_2$	18.9	3.7854	9.5112	136.29
0.28 mol.%Ce/TiO$_2$	13.2	3.7870	9.5113	136.41
3 mol.%Ce/TiO$_2$	8.6	3.7886	9.509	136.49
5 mol.%Ce/TiO$_2$	8.9	3.7907	9.510	136.65
10 mol.%Ce/TiO$_2$	10.4	3.7920	9.507	136.70

[a] The volume weighted TiO$_2$ anatase crystallite size.

44.2° and 56.4°, respectively, also (1 0 3) and (1 1 2) $h\,k\,l$ reflections at 43.2° and 45.1° are evident. Compared to cerium doped TiO$_2$, for which both these reflections are not evident, this indicates that anatase crystallites in parent TiO$_2$ are markedly larger than in other investigated photocatalysts. Any evident diffraction lines from ceria crystalline phase are not observed in cerium doped TiO$_2$ photocatalysts and, in addition, it is visible that with increasing Ce loading the anatase reflections appear less intense. These observations indicate that cerium in Ce-loaded TiO$_2$ photocatalysts is probably present as the ceria amorphous phase and the degree of crystallinity of individual photocatalysts as well as the titania crystallite-size depends on the Ce loading. The effect of Ce loading on the TiO$_2$ anatase crystallite-size is depicted in Fig. 3b and summarized in Table 2.

Concerning the possible inhibiting effect of cerium on the growth of TiO$_2$ crystallites and the TiO$_2$ phase transformation, which correlates vice versa, our conclusion can be supported by literature [43,44]. Lin et al. [43] justified the stabilization of TiO$_2$ anatase by surrounding Ce ions based on the formation of Ti—O—Ce bonds at the TiO$_2$–CeO$_2$ interface. Fang et al. [44] proposed that the CeO$_2$ clusters preferentially nucleate on the oxygen vacancies within TiO$_2$ anatase, which forms the interface bridged with oxygen between CeO$_2$ and anatase. At low Ce contents this occurs preferentially on the oxygen vacancy sites in the bulk of TiO$_2$ anatase
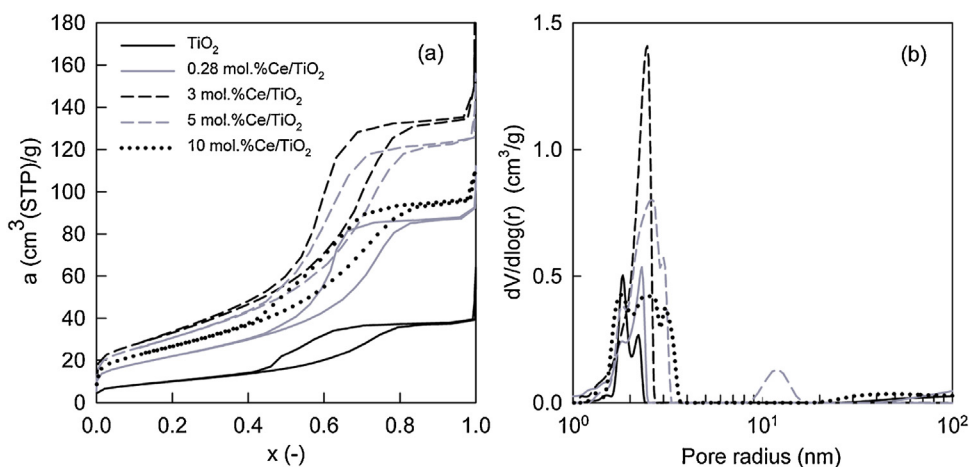

Fig. 2. (a) The measured nitrogen adsorption-desorption isotherms and (b) evaluated pore-size distributions of investigated photocatalysts.
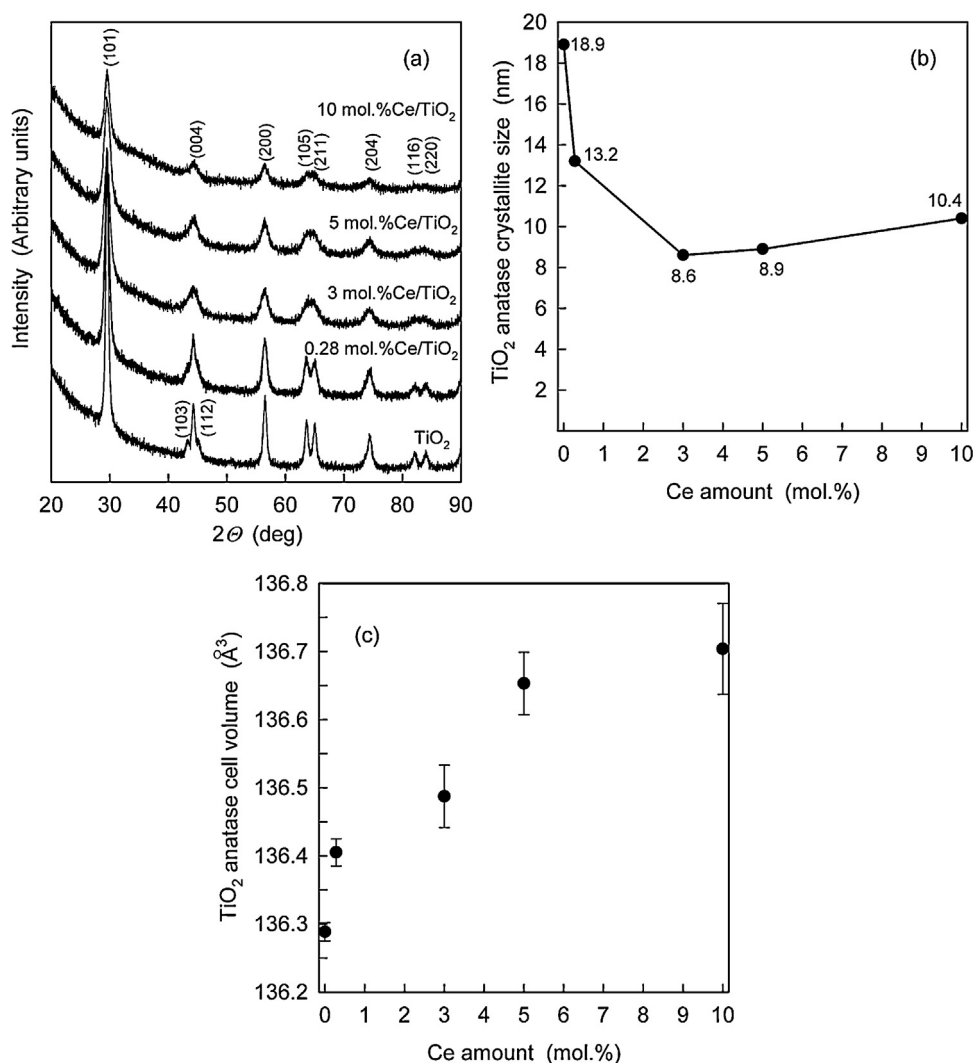
Fig. 3. (a) XRD patterns of investigated photocatalysts, (b) the correlation between the Ce amount and the TiO_2 anatase crystallite-size and (c) the correlation between the Ce amount and the anatase cell volume.

than on its surface, because surface oxygen vacancy sites are preferably hydroxylated and thus filled. With the increasing Ce content the CeO_2 clusters grow, forming cubic CeO_2 crystallites. Hence, the decreasing concentration of oxygen vacancies and the Ti—O—Ce interface are responsible for the inhibition of structural changes within TiO_2 anatase in TiCe mixed oxides. It is not therefore surprising, that the anatase crystallite-size decreases with increasing Ce content, as it is nicely depicted in Fig. 3b and summarized in Table 2 for the TiO_2 photocatalysts with Ce loading up to 3 mol.%.

The volume weighted crystallite size of anatase decreased from 18.9 nm for the pure TiO_2 photocatalyst to 8.6 nm for the 3 mol.%Ce/TiO_2 photocatalyst. However, it is quite surprising that the decreasing trend in anatase crystallite-size does not continue up to 10 mol.% Ce loading. The TiO_2 crystallites slightly increase their size to 8.9 nm and 10.4 nm for the Ce loadings 5 mol.% and 10 mol.%, respectively. In addition, especially for 10 mol.%Ce/TiO_2, the significant decrease of intensity of XRD reflections can be noticed (Fig. 3a). The unexpected phenomenon within the TiO_2 anatase crystallite-size in the 5 mol.% Ce/TiO_2 and 10 mol.%Ce/TiO_2 photocatalysts can be partially explained based on our previous study [26], in which the in-situ XRD measurements were carried out with 10 mol.%Ce/TiO_2 and individual high-quality XRD spectra (measured using CuKα radiation) were investigated in detail by using the advanced XRD whole powder pattern modeling [45]

implemented in software MStruct [35]. Besides the main anatase (1 0 1) hkl reflection, the weak broad peak was identified on the background of XRD spectra for the broad temperature range 350–600 °C. This weak broad diffraction line corresponded to the presence of very small CeO_2 crystallites (~1 nm). Moreover, it was evaluated that besides TiO_2 anatase, some amorphous TiO_2 is also present [26]. With respect to this knowledge and the facts that (i) the 10 mol.%Ce/TiO_2 sample in this study was prepared by using the same sol–gel procedure, nevertheless, the slightly different calcination regime and (ii) the presented XRD spectra were not measured at so high resolution as previously, it can be reasonably speculated about the real form of ceria in 10 mol.%Ce/TiO_2. In spite of the fact that according to the XRD pattern 10 mol.% of Ce in TiO_2 results ostensibly in the photocatalyst with the amorphous ceria, the CeO_2 cubic crystallites can nucleate in the bulk of TiO_2 anatase. However, they do not have to be detected by XRD because they are very small and thus beyond XRD detection limit. Moreover, the detection of such small ceria crystallites in the bulk of TiO_2 is more difficult in the case of our photocatalyst due to the presence of some amorphous TiO_2. The same crystallization phenomenon, however, significantly less pronounced due to markedly lower Ce amount, occurs also for 5 mol.% Ce/TiO_2. It is worth a mention that our considerations are in an agreement with Fang et al. [44] who also reported about the effect of Ce amount on the nucleation of
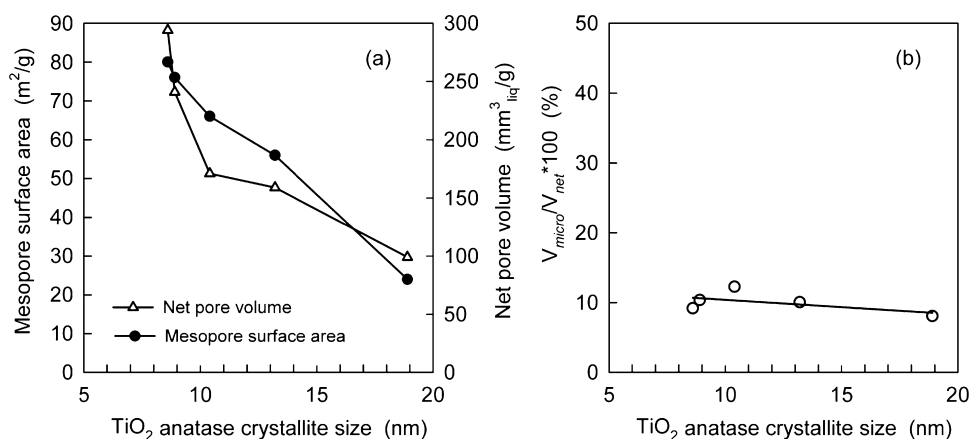
Fig. 4. The correlations between (a) the mesopore surface area as well as the net pore volume of catalysts and the TiO_2 anatase crystallite-size and (b) the microporosity of catalysts and the TiO_2 anatase crystallite-size.

CeO_2 cubic phase in the mixture with TiO_2 anatase and the problematic detection of formed very small CeO_2 crystallites by using XRD and even visible- and UV-Raman spectroscopy. Moreover, this theory about initial nucleation of ceria in the 5 mol.%Ce/TiO_2 and 10 mol.%Ce/TiO_2 photocatalysts can be supported by formerly discussed textural properties (Table 1), when the net pore volume as well as the surface area of the 5 mol.%Ce/TiO_2 and 10 mol.%Ce/TiO_2 photocatalysts are decreased compared to 3 mol.% Ce/TiO_2.

Since textural properties are closely connected with structural properties, this nicely correlates to slightly increased TiO_2 anatase crystallite-size (8.9 nm and 10.4 nm for 5 mol.%Ce/TiO_2 and 10 mol.%Ce/TiO_2, respectively) (Table 2). The correlation between the surface area as well as the net pore volume of catalysts and the anatase crystallite-size is depicted in Fig. 4a. The correlation between the microporosity of catalysts and the anatase crystallite-size is depicted in Fig. 4b. It can be seen that while the catalyst mesopore surface area and the net pore volume decreases with increasing TiO_2 anatase crystallite-size, the microporosity stays practically constant (8–12%) within the whole range of anatase crystallite size 8–19 nm. It reveals that the mesoporosity of catalysts may be preferentially attributed to voids existing between individual crystallites and thus can be influenced by changes in crystallite size.

Considering the literature [11,44], it should be also noticed that, whether the CeO_2 cubic phase appears in the mixture with anatase, it strongly depends on the loaded Ce molar amount as well as the used preparation procedure. Fang et al. [44] who prepared cerium doped TiO_2 using an acid catalyzed sol–gel method reported that only anatase is formed below 0.5 wt.% of Ce and TiO_2–CeO_2 mixed oxide appears above 0.5 wt.% of Ce. Pavasupree et al. [11] who synthesized TiO_2-CeO_2 mixed oxides by using a surfactant–laurylamine hydrochloride–assisted sol–gel method observed the same trend in crystallization of pure TiO_2 and 5 mol.%Ce/TiO_2 as in our study. For 10 mol.%Ce/TiO_2 the mixture of cubic CeO_2 and anatase already crystallized. Thus, based on these facts and own results it seems that the used preparation method itself strongly influences the crystallization of TiO_2–CeO_2 mixed oxides and by using surfactants mediated sol–gel method the CeO_2 cubic phase crystallizes besides anatase at higher Ce molar content ($\geq$10 mol.%) and higher temperature than when using acids catalyzed sol–gel method.

Incorporation of Ce^{4+} ions into TiO_2 lattice–the impact on structural properties of cerium doped TiO_2, explanation based on XRD and Raman spectroscopy

Based on above mentioned facts about the evolution of structural and textural properties of individual photocatalysts

(Tables 1 and 2 and Fig. 3a,b) the interesting discussion, concerning the possible substitution of Ti^{4+} ions within anatase crystal structure by Ce^{4+} ions, the formation of amorphous CeO_2 and its crystallization to cubic crystal structure, arises. López et al. [46] simulated the crystal structure of Ce-doped anatase lattice to examine the possible substitution of Ti^{4+} by Ce^{4+} ions, since Ce^{4+} ions (0.92 Å) are larger than Ti^{4+}(0.68 Å) [44]. They reported that the anatase crystalline structure includes interstitial channels in which Ce^{4+} coordinated species can gain access in order to substitute some Ti^{4+} moieties. When linear or branched $\equiv$Ti—O^- chains are formed in the sol state, Ce^{4+} can be inserted between these chains by direct linking or by substitution of one Ti^{4+} to finally obtain $\equiv$Ti—O—Ce—O—Ti$\equiv$ solid arrangement. They stated that the whole TiO_2 network can be saturated with relatively small amount of Ce (in a consequence of the relatively large difference between atomic radii of Ti^{4+} and Ce^{4+} ions), the rest of Ce is found dispersed on the surface as CeO_2. From XRD data they calculated the unit cell parameters of pure TiO_2 and the 10 wt.%Ce/TiO_2 sample calcined at different temperatures, which both possessed only anatase crystal structure for the temperature range 200–600 °C, and they observed the expansion of the anatase unit cell for the sample doped by Ce, compared to pure TiO_2. This result basically proved the possible substitution of Ti^{4+} in anatase lattice by Ce^{4+} ions. Moreover, this conclusion was confirmed by the crystal structure simulation which confirmed that from the stereo-chemical point of view the inclusion of Ce^{4+} to anatase lattice is possible [46].

In general, the increasing content of Ce (from 0.28 to 10 mol.%) in TiO_2 led to the expansion of anatase cell volume (Table 2, Fig. 3c). However, it can be seen that the anatase cell volume increased monotonically only in the range of 0.28–5 mol.% of Ce and it limited to constant value from 5 mol.% of Ce (Fig. 3c). This trend likely supports above mentioned speculation about the formation/separation of amorphous ceria and its possible nucleation for the samples containing more than 5 mol.% of Ce. The increase of anatase cell volume to ~5 mol.% of Ce corresponds to the fact that the occupation of anatase lattice by Ce^{4+} ions takes place. Around ~5 mol.% of Ce loading the TiO_2 lattice is already saturated by Ce^{4+} ions and the separation/formation of CeO_2, either as amorphous phase or very small nuclei, occurs.

Since the Raman spectroscopy is very sensitive method of analysis regarding the crystallinity, it was used to reveal the influence of different Ce molar contents on the FWHM and the shift of $E_{g(1)}$ and $E_{g(3)}$ anatase bands (145 and 641 cm^{-1}) for the investigated samples. TiO_2 as well as all cerium doped TiO_2 showed in Raman spectra only bands centered to 145, 399, 520 and 641 cm^{-1}, characteristic to the Raman-active modes of TiO_2 anatase with the symmetries of $E_{g(1)}$, B_{1g}, A_{1g} and $E_{g(3)}$ [47] (Fig. 5a). For the 10 mol.%Ce/TiO_2
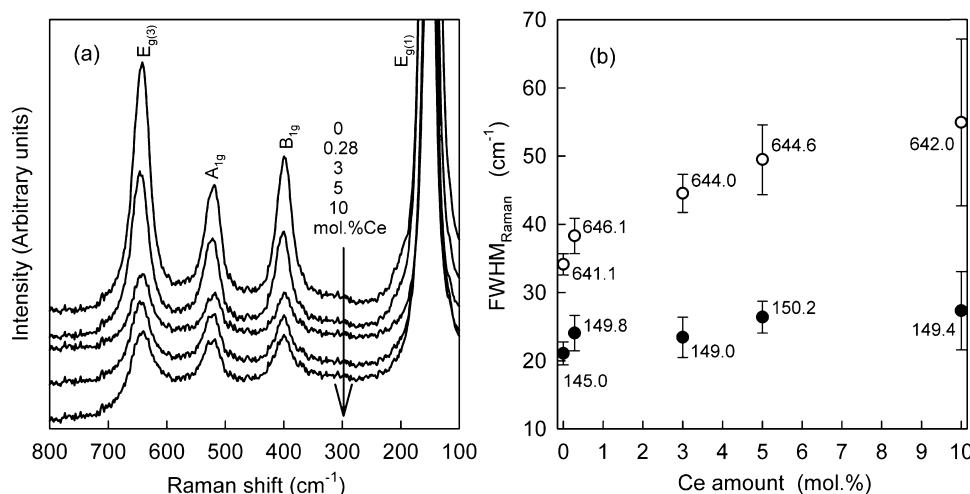
Fig. 5. (a) Raman spectra of investigated photocatalysts and (b) the correlation between the Ce amount and Raman FWHM of $E_g(1)$ and $E_g(3)$ TiO_2 anatase bands (145 and 641 cm^{-1}). ●$E_g(1)$ band, ○ $E_g(3)$ band.

photocatalyst these bands were additionally superimposed with a broad feature between 900 and 100 cm^{-1}, indicating the presence of some amorphous phase. Any band from cubic CeO_2, even its strong band at ~463 cm^{-1}, was not presented in the recorded spectra. The cubic CeO_2 possesses six optical-phonon branches, but generally only the Raman mode at ~463 cm^{-1} viewed as a symmetric breathing of the oxygen ions around Ce ions can be directly detected by spectral measurement [48].

The key results from Raman spectroscopy are shown in Fig. 5b. It can be seen that the FWHM of anatase $E_{g(1)}$ band (145 cm^{-1}) as well as $E_{g(3)}$ band (641 cm^{-1}) changes with increasing Ce content in the range 0.28–10 mol.% (Fig. 5b). The anatase $E_{g(3)}$ band is evidently more sensitive to the loaded Ce amount. While for anatase $E_{g(1)}$ band the change of FWHM with increasing Ce amount in the range 0.28–10 mol.% compared to pure TiO_2 is only negligible (ΔFWHM is within 2.4–6.5 cm^{-1}) and the FWHM of the band keeps practically constant, the FWHM of $E_{g(3)}$ band increases significantly. ΔFWHM of $E_{g(3)}$ band is within 4.4–21 cm^{-1} for 0.28–10 mol.% of Ce, which is, moreover, accompanied with the markedly increased FWHM variance at 5 mol.% and 10 mol.% of Ce. This feature indicates structural changes within TiO_2 anatase and its close surroundings at higher Ce molar contents and nicely correlates with the assumed presence of CeO_2 amorphous phase/progressing ceria nucleation. The markedly increased FWHM variance can be even seen at 10 mol.% of Ce for the anatase less-structural sensitive $E_{g(1)}$ band. It should be noticed that the probable structural changes concerning CeO_2 in the mixture with anatase in our case also reflects to the Raman shift of more sensitive anatase $E_{g(3)}$ band. With increasing Ce content from 0.28 to 10 mol.% the anatase $E_{g(3)}$ band shifts from ~646 cm^{-1} to ~642 cm^{-1}, which is close to the position of anatase $E_{g(3)}$ band in undoped TiO_2 (~641 cm^{-1}, Fig. 4b). This could be in agreement with the phenomenon described by López et al. [46] who reported that the anatase lattice is being saturated by Ce^{4+} ions and then the separation of CeO_2 dispersed on titania surface takes place. The explanation, why the position of $E_{g(1)}$ band does not change anyway within different Ce loading, is its generally markedly lower sensitivity with respect to progressing structural changes.

Surface properties

To study the surface chemical composition of Ce-doped TiO_2 photocatalysts the XPS spectra were measured. The XPS survey spectra evidence that only expected elements: Ti, Ce, O and C were present on the surface of all examined photocatalysts. In Table 3 the results of XPS analysis are demonstrated. It should be kept in mind that carbon detected on the surface (at similar content for all tested samples) corresponds to carbon-based contamination, and the binding energy (284.6 eV) of main C 1s line was applied to charge correction. The O 1s spectra were deconvoluted into three distinct peaks: the first one with the lowest binding energy (~529.5 eV) can be assigned to lattice oxygen in metal oxides, the second one (~531.0 eV) can be ascribed to the chemisorbed oxygen or/and hydroxyl species and the third one at the highest binding energy (~534.1 eV) corresponds to water adsorbed on the surface [44,49–51]. It can be seen that with decreasing Ce loading the content of chemisorbed oxygen or/and hydroxyl species increases from 6.9 to 17.3 at.%. In all examined cerium doped TiO_2 photocatalysts the binding energies of Ti 2p 1/2 and Ti 2p 3/2 are about 464.0 eV and 458.3 ± 0.1 eV, respectively. This indicates that significantly different Ce amounts do not influence the Ti 2p binding energies and Ti exists as Ti^{4+} in the studied solids. The identification of chemical states of Ce was done based on the Ce 3d 3/2 and Ce 3d 5/2 peaks, which were deconvoluted according to the convention established by Burroughs et al. [52]. The peaks at the highest binding energy, representing the final state of Ce^{4+} $3d^9 4f^0$ O $2p^6$, were used to distinguish Ce^{4+} and Ce^{3+}, because they are not observed for trivalent ionic cerium compounds [53–56]. For all studied samples the mixture of Ce^{3+} and Ce^{4+} oxidation states was found. Nevertheless, with the decreasing Ce content in TiO_2 the relative content of Ce^{3+} ions on the photocatalyst surface increases from 36.7 to 73% (Table 3). The determined surface properties such as the existence of Ce^{3+}/Ce^{4+} oxidation states on the surface and the increased amount of the chemisorbed oxygen or/and hydroxyl species at lower Ce amount seem to be ones of key parameters from the view of latter explanation of the catalyst performance in the CO_2 photoreduction, because Wang et al. [24] suggested that just these properties may contribute to the enhanced activity of the ordered mesoporous CeO_2–TiO_2 composites in this reaction.

Optical properties

The UV–vis diffuse reflectance spectra of TiO_2 and Ce-doped TiO_2 photocatalysts were taken in order to investigate their spectral response. It can be proved that the modification of TiO_2 with cerium affected significantly the absorption properties of photocatalysts (Fig. 6a and b). The absorption edge at 3.19 eV for TiO_2 (Fig. 6b) can be likely attributed to the band-gap excitation of anatase. The red shift of the absorption edge to the visible region for cerium doped TiO_2 materials was observed. The spectra shift more to the visible region with the increasing amount of Ce in Ce/TiO_2 materials.

Table 3
Surface properties of investigated photocatalysts determined by using XPS.

Photocatalyst	Ti 2p	C 1s	O 1s				Ce 3d			
	Ti^{4+} (at.%)	C_{ad} (at.%)	M—O (at.%)	M—OH, O_{chem} (at.%)	H_2O_{ads} (at.%)	Sum (at.%)	Ce^{3+} (at.%)	Ce^{4+} (at.%)	Sum (at.%)	$Ce^{3+}/(Ce^{3+}+Ce^{4+})$ (%)
3 mol.%Ce/TiO_2	25.74	11.09	44.32	17.26	0	61.58	1.16	0.43	1.59	73.0
5 mol.%Ce/TiO_2	23.10	10.21	45.00	11.78	7.61	64.39	1.28	1.02	2.30	55.7
10 mol.%Ce/TiO_2	22.20	10.32	50.23	6.85	5.33	62.41	1.85	3.19	5.04	36.7

The 0.28 mol.%Ce/TiO_2 photocatalyst was not analyzed because of XPS detection limit.

Moreover, a significant increase in the absorption was observed between 3.19 eV (389 nm) and 2.64 eV (470 nm), which increases with increasing Ce loading. Fig. 6c shows the dependence of the absorption edge on the Ce loading. It can be seen that the small Ce loadings (to ~1 mol.%) in TiO_2 leads to a steep linear decrease of the absorption edge from 3.19 eV (for TiO_2) to 2.79 eV (for ~1 mol.% of Ce in TiO_2). This decrease in the absorption edge continues up to ~3 mol.% of Ce. With further increasing Ce loading the absorption edge slowly limits to approximately 2.64 eV for 10 mol.% of Ce. CeO_2 is a *n*-type semiconductor whose band gap vary from 2.7 to 3.4eV depending on the preparation method [57,58]. The red shift of Ce-loaded TiO_2 materials is still a matter of a discussion. Jiang et al. [59] observed decreasing value of the absorption edge (from 3.2 eV to 2.6 eV) with decreasing thickness of nanocrystalline CeO_2 films (from 334 to 41 nm). Previously, the red shift of Ce/TiO_2 materials has been attributed to the new energy level in the band gap of Ce/TiO_2 materials in contrast to the TiO_2 [60] and to the electrons

excitation from the valence band of TiO_2 or ground state of cerium oxides to Ce 4f level [61].

3.2. The photocatalytic reduction of CO_2

The effect of irradiation time on the formation of products in the CO_2 photocatalytic reduction was investigated over TiO_2 as well as over different cerium loaded TiO_2 catalysts. Fig. 7 shows the evolution of reaction products as the function of irradiation time for the TiO_2 catalyst. Methane and hydrogen were recognized as the gaseous products of reaction. Other products such as carbon monooxide, methanol, formic acid, formaldehyde, ethane and ethylene may also be formed, but they were not detected. The ranking of products yields (in μmol/g-cat.) was following: $H_2 > CH_4$.

The products yields from longer reaction time span (i.e. 18 h) were chosen for the comparison of individual photocatalysts performance because the yields were higher and thus more accurate
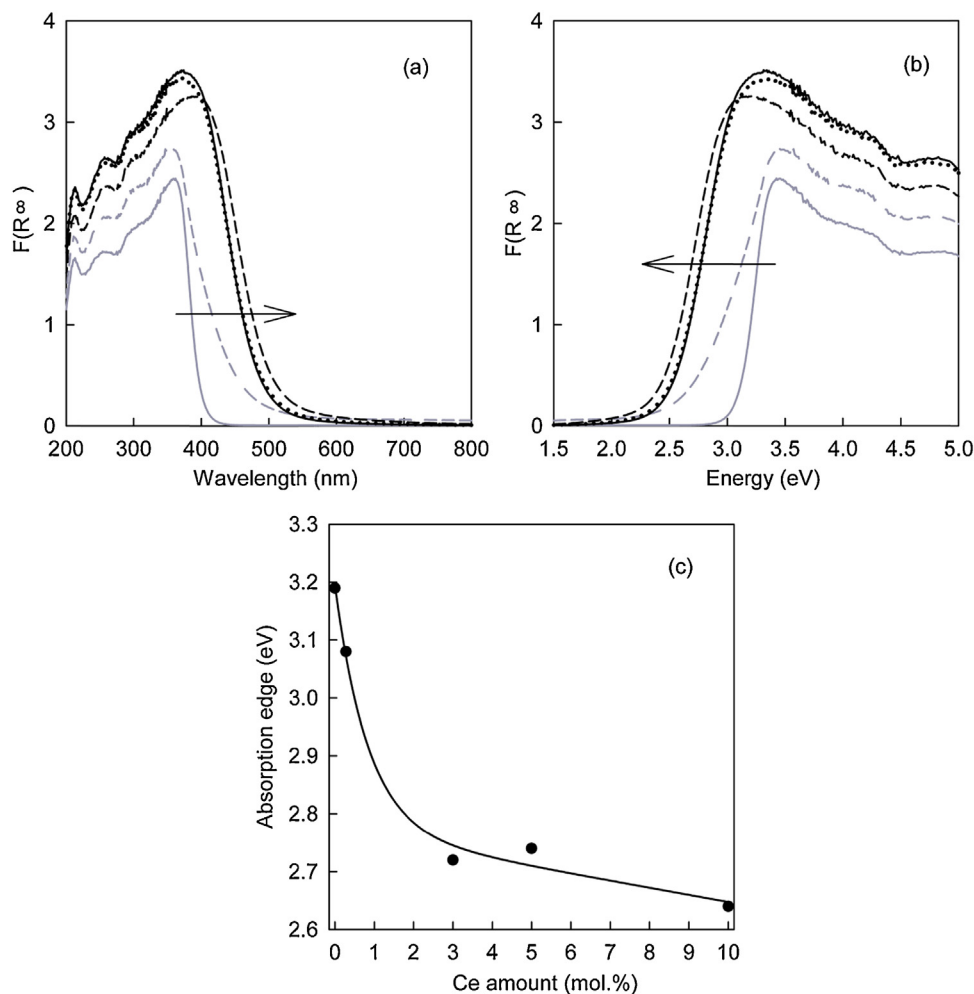

Fig. 6. (a,b) UV–vis DRS spectra of investigated photocatalysts and (c) the correlation between the Ce amount and the absorption edge energy. TiO_2 (solid grey), 0.28 mol.%Ce/TiO_2(dash grey), 3 mol.%Ce/TiO_2(dotted black), 5 mol.%Ce/TiO_2 (solid black), 10 mol.%Ce/TiO_2(dash black).
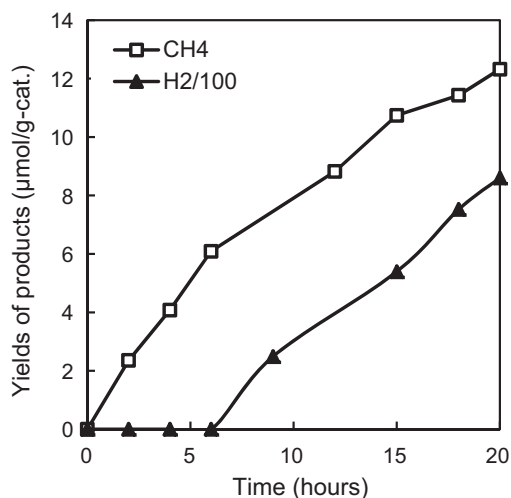
Fig. 7. The time dependence of the products yields over the TiO_2 catalyst.

Fig. 9. The dependence of methane yields on the TiO_2 anatase crystallite-size.

and reliable. The effect of cerium doping on the yields of the main products (methane and hydrogen) related to the weight of the catalyst is depicted in Fig. 8a and b. The photoreactivity of cerium doped TiO_2 catalysts decreases with increasing Ce dopant concentration. Yields of both reaction products are the highest for the 0.28 mol.%Ce/TiO_2 photocatalyst.

Fig. 9 shows the dependence of the yields of methane on the anatase crystallite size. The photocatalysts with 5 and 10 mol.% of Ce are not included in Fig. 9 because of the presence of amorphous ceria. It can be seen that the maximum yield of methane was reached for the photocatalyst with the anatase crystallite-size of 13.2 nm of the 0.28 mol.%Ce/TiO_2 catalyst. This finding pretty correlates with our previous works [39,62] where the maximum products yields of CO_2 photocatalytic reduction were observed for the anatase crystallite size in the range 12–14 nm.

3.3. Aspects influencing the photocatalytic reduction of CO_2 over Ce doped TiO_2

There are several aspects influencing the photocatalytic performance of nanoparticles such as the absorption edge, surface area and surface properties and most importantly electron and hole energies. All these aspects can be significantly positively affected by the addition of Ce into TiO_2 anatase matrix, since it (i) decreases
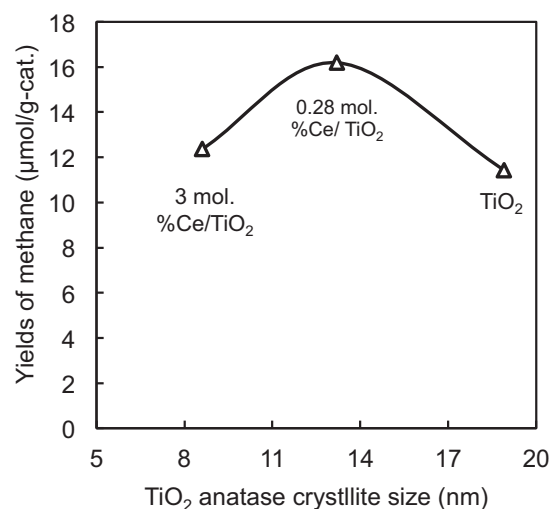
the anatase nanoparticle size (Fig. 3b) and consequently increases the photocatalytic surface area (Table 1), (ii) decreases the band gap energy (Fig. 6c) increasing so the effectivity of electron–hole pair generation due to the absorption of lower energy photons and (iii) retards the fast charge recombination. The surface area was discussed in the Section 3.1, so in following discussion the remaining aspects (ii) and (iii) will be discussed as well.

Electron and hole energies and visible light absorption

In our case the electron energy in conduction band must be higher than H^+ reduction potential and the hole energy in valence band must be lower than OH^- oxidation potentials. Pure TiO_2 anatase crystal structure has itself the conduction band energy sufficient, but very close to H^+ reduction potential. Since Ce atoms are larger than Ti atoms, the addition of Ce atoms into TiO_2 crystal structure should result in the band gap decreasing and lower absorption edge energies can be expected and it was also experimentally demonstrated (see Fig. 6). However, it is always difficult to predict separately the shift of conduction and valence band energies, which are extremely important with respect to required oxidation and reduction potentials. The knowledge of nanoparticles work function for different Ce loadings shown in Fig. 10 can help us to elucidate the shift of conduction as well as valence bands. For simplicity, it can be supposed that the Fermi level on nanoparticle
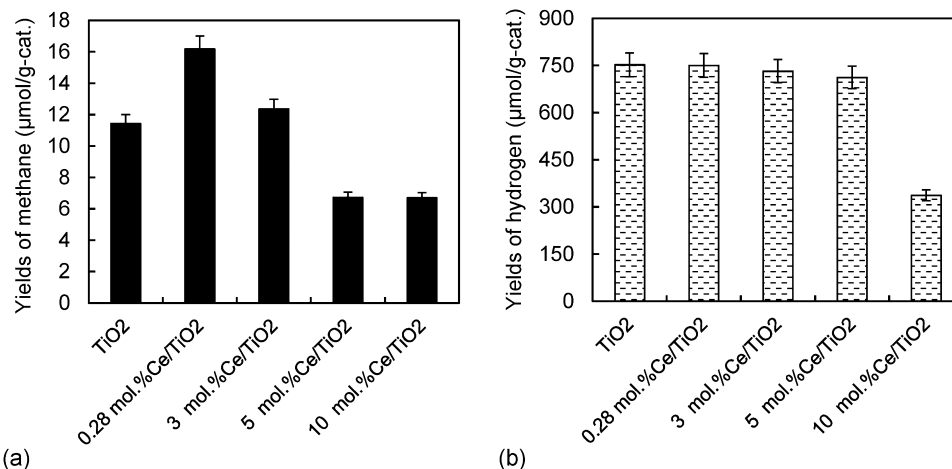

(a)

(b)

Fig. 8. Yields of (a) methane and (b) hydrogen over individual investigated photocatalysts in the CO_2 photocatalytic reduction (related to the weight of catalyst). Conditions: 18 h of irradiation time, 8 W Hg lamp, CO_2 pressure at carbonation of 110 kPa, 100 ml of H_2O, catalyst concentration of 1 g/l, pH 5.
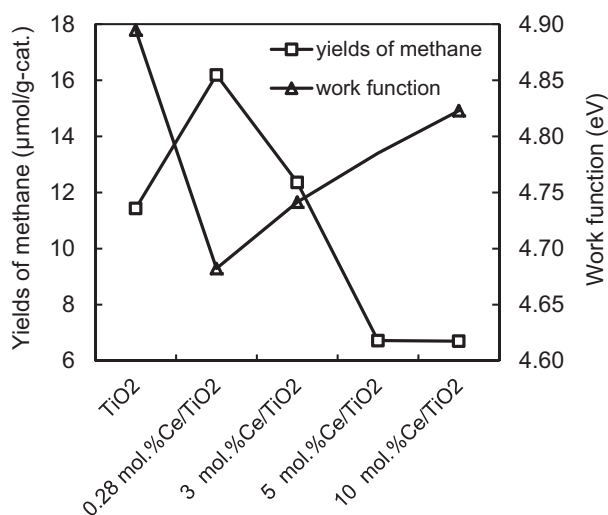
Fig. 10. The correlation between methane yields and the work function for investigated photocatalysts.

surface is pinned to the middle of nanoparticle band gap. This simplification allows us high density of charged states on nanoparticles surface. Deriving from Figs. 6 and 10 and Table 1 it can be estimated that the energy of electrons on the conduction band edge increases by approximately 145 meV, while the valence band edge shifts up by ~255 meV for 0.28 mol.%Ce/TiO$_2$ nanoparticles with respect to the values for pure TiO$_2$ anatase. Since the pure anatase valence band energy is approximately 500 meV lower than required oxidation potential of holes, the hole energy in 0.28 mol.%Ce/TiO$_2$ nanoparticles is sufficient for oxidation of hydroxyl anions. It can be concluded that for 0.28 mol.%Ce/TiO$_2$ nanoparticles both carriers have sufficient potentials for the photocatalytic reaction (Fig. 11).

Similar considerations for 3 mol.%Ce/TiO$_2$ nanoparticles give approximately 310 meV increase of hole energy in the valence band and 75 meV decrease of electron energy in the conduction band with respect to the values of pure anatase. Since the pure TiO$_2$ anatase crystal structure has the conduction band energy sufficient very close to H$^+$ reduction potential, the decrease of electron energy is critical for the photocatalytic performance. For 3 mol.%Ce/TiO$_2$ nanoparticles the electron energy in conduction band decreases slightly below H$^+$ reduction potential, thus the photocatalytic performance of such a catalyst is decreasing. For 10 mol.%Ce/TiO$_2$ nanoparticles the decrease of electron energy in the conduction
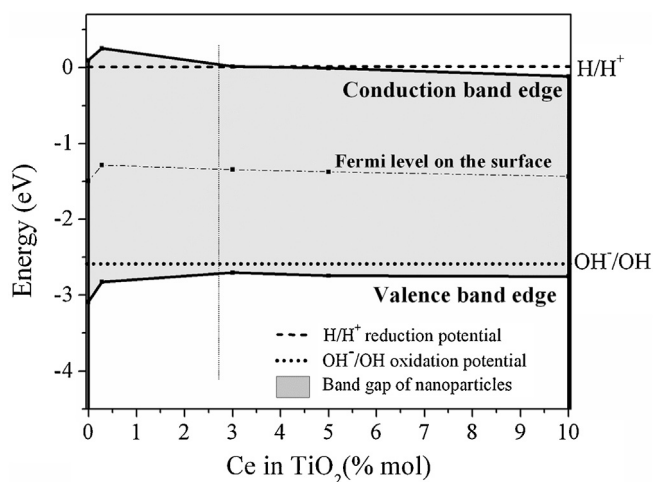

Fig. 11. Illustration of the shifts of energies of electrons and holes in conduction and valence bands in dependence on the Ce loading.

band is even ~202 meV with respect to the values of pure anatase (Fig. 11) which is deeply below H$^+$ reduction potential, correlating with the lowest photocatalytic performance.

Combining the information about the work function (Fig. 10) with band gap energies for different Ce loadings (Fig. 6 and Table 1), the optimal Ce content which will maximally lower the band gap energy while keeping sufficient electron and hole potentials may be estimated to ~2 mol.% of Ce in TiO$_2$.

Retardation of the fast charge recombination

The doping with various Ce loadings also influences surface properties of TiO$_2$ based photocatalysts such as (i) a level of surface coverage by CeO$_2$, (ii) a ratio of present Ce^{3+}/Ce^{4+} species or (iii) the presence of surface oxygen species (i.e. the chemisorbed oxygen and/or hydroxyl groups on the catalyst surface) and, thus, in final the photocatalytic/solar-light performance. Wang et al. [24] who studied the CO$_2$ reduction under solar light reported on the fact that the surface oxygen species on the CeO$_2$–TiO$_2$ composite surface can easily capture electrons and yield surface oxygen radicals with excellent reduction capability. Besides that, Ce^{3+} ions could interact with holes and prevent the recombination of photogenerated electrons and holes, resulting in a higher catalytic performance. In their study the CeO$_2$–TiO$_2$ composites with the molar ratio of Ce/Ti ~1 and 0.5 was found out as the most catalytically active. In our study the catalyst performance in the CO$_2$ photoreduction is decreasing in ranking: 0.28 mol.%Ce/TiO$_2$ > 3 mol.%Ce/TiO$_2$ > TiO$_2$ > 5 mol.%Ce/TiO$_2$ > 10 mol.%Ce/TiO$_2$. This trend indicates the existence of optimum Ce loading for catalysts working under UV light and with this fact also corresponding ability of the Ce^{3+}/Ce^{4+} redox couple to reduce the recombination by enabling faster electron transfer along the TiO$_2$ surface [58,63–65]. The explanation, why the Ce ions can reduce the recombination of the charge carriers, enhancing the performance under the UV light, was reported following [58]: the required potential for reduction of Ce^{4+} to Ce^{3+} is +1.61 V (vs. NHE) and for oxidation of Ce^{3+} to Ce^{4+} is −1.61 V (vs. NHE). The conduction band (CB) of TiO$_2$ possesses a potential −0.29 V which is more negative than that of Ce^{4+} to Ce^{3+} reduction potential. Therefore, the CB electrons of TiO$_2$ are able to reduce Ce^{4+} to Ce^{3+}. The valence band (VB) of TiO$_2$ has a potential of +2.91 V which is more positive than of Ce^{3+} to Ce^{4+} oxidation potential. The VB hole can hence oxidize Ce^{3+} to Ce^{4+}. These reduced Ce^{3+} and oxidized Ce^{4+} species can subsequently transfer the charges to the species present in the reaction medium [65]. According to XPS survey study for our Ce/TiO$_2$ nanoparticulated materials (Table 3) it is evident that with increasing Ce loading the population of Ce^{3+} ions on the catalyst surface markedly decreases from 73 to 37%, assuming the maximum Ce^{3+} ions population for 0.28 mol.% Ce loading. However, in our case the retardation of fast charge recombination by Ce^{3+}/Ce^{4+} redox couple is not the phenomenon responsible for the trend in photocatalytic performance of mentioned Ce/TiO$_2$ materials, since based on DR UV–vis and contact potential difference measurements it was experimentally revealed that different Ce loading in TiO$_2$ nanoparticles affects crucially the energy of holes in valence band and especially electrons in conduction band and these properties directly influence the CO$_2$ photoreduction (Fig. 11). At higher Ce loadings (≥3 mol.%) in TiO$_2$ nanoparticles the energy of electrons in conduction band decreases below required H$^+$ reduction potential and thus the performance of these materials in CO$_2$ photoreduction is decreasing.

4. Conclusions

The parent TiO$_2$ and cerium doped TiO$_2$ photocatalysts with Ce loadings within 0.28–10 mol.% were prepared by the sol–gel method controlled within reverse micelles of nonionic surfactant

Triton X-114, were comprehensively characterized using several complementary investigation methods and their performance was explored for the CO_2 photocatalytic reduction. Cerium doped TiO_2 photocatalysts with Ce loadings from 0.28 to 10 mol.% were investigated for this type of reaction for the first time.

Concerning the structural and microstructural properties of photocatalysts, it was proved that the addition of cerium inhibits the growth of TiO_2 crystallites. However, it was revealed that the inhibiting effect of cerium on the TiO_2 crystallites growth occurred only up to 3 mol.% of Ce when the incorporation of Ce^{4+} into the anatase lattice took place. This fact nicely corresponded to the expansion of anatase cell volume. At higher Ce loadings (≥ 5 mol.%) the anatase lattice was saturated by Ce^{4+} ions and the formation/separation of amorphous ceria and/or ceria (~ 1 nm) nucleation occurred, accompanied with the increase of TiO_2 anatase crystallite-size and the limitation of value of anatase cell volume. The increased surface concentration of Ce^{4+} ions at higher Ce loadings was confirmed by XPS analysis.

The correlation between textural and structural properties of Ce/TiO_2 nanoparticulated photocatalysts was found out. It was revealed that the mesoporosity of photocatalysts may be preferentially attributed to voids existing between individual crystallites and thus can be influenced by changes in crystallite size.

The modification of TiO_2 with cerium also affected the spectral response of photocatalysts, shifting it to the visible light region. The absorption edge of photocatalysts was decreasing with increasing Ce loading, from 3.19 eV (for TiO_2) up to 2.64 eV (for 10 mol.%Ce/TiO_2). However, in final this property itself was not crucial in the photocatalytic CO_2 reduction.

The key role in the performance of cerium doped TiO_2 materials in the CO_2 photocatalytic reduction played the energies of electrons and holes within the electronic structure of designed photocatalysts, which were markedly affected by the Ce atoms addition. For 0.28 mol.%Ce/TiO_2, both electrons and holes have required potentials for the photocatalytic reduction of CO_2, while for 3 mol.%Ce and higher Ce loading in TiO_2 nanoparticles the energy of electrons is bellow H^+ reduction potential and thus the photocatalytic performance of these catalysts is decreasing.

From the measured dependencies of work function and band gap energies on the Ce loading in TiO_2 the optimal Ce content in TiO_2 anatase, which will maximally lower the band gap energy while keeping sufficient electron and hole potentials to enter the photocatalytic reactions, may be estimated to ~ 2 mol.% of Ce.

Acknowledgements

References

[1] A. Verma, A. Goyal, R.K. Sharma, Thin Solid Films 516 (2008) 4925–4933.
[2] A. Verma, S.B. Samanta, N.C. Mehra, A.K. Bakhshi, S.A. Agnihotry, Sol. Energy Mater. Sol. Cells 86 (2005) 85–103.
[3] A. Verma, S.B. Samanta, A.K. Bakhshi, S.A. Agnihotry, Solid State Ionics 171 (2004) 81–90.
[4] F.E. Ghodsi, F.Z. Tepehan, G.G. Tepehan, Electrochim. Acta 44 (1999) 3127–3136.
[5] M.R. Mohammadi, D.J. Fray, Sensors Actuat. B 150 (2010) 631–640.
[6] A. Trinchi, Y.X. Li, W. Wlodarski, S. Kaciulis, L. Pandolfi, S. Viticoli, E. Comini, G. Sberveglieri, Sensors Actuat. B 95 (2003) 145–150.
[7] X. Zhao, Q. Zhao, J. Yu, B.J. Liu, J. Non.-Cryst. Solids 354 (2006) 1424–1430.
[8] H.Q. Zhu, Z.F. Qin, W.J. Shan, W.J. Shen, J.G. Wang, J. Catal. 225 (2004) 267–277.
[9] A.K. Sinha, K. Suzuki, J. Phys. Chem. B 109 (2005) 1708–1714.
[10] B.S. Liu, X.J. Zhao, N.Z. Zhang, Q.N. Zhao, X. He, J.Y. Feng, Surf. Sci. 595 (2005) 203–211.
[11] S. Pavasupree, Y. Suzuki, S. Pivsa-Art, S. Yoshikawa, J. Solid State Chem. 178 (2005) 128–134.
[12] Z. Liu, B. Guo, L. Hong, H. Jiang, J. Phys. Chem. Solids 66 (2005) 161–167.
[13] B. Jiang, S. Zhang, X. Guo, B. Jin, Z. Tian, Appl. Surf. Sci. 255 (2009) 5975–5978.
[14] F. Galindo, R. Gómez, M. Aguilar, J. Mol. Catal. A: Chem. 281 (2008) 119–125.
[15] S. Otsuka-Yao-Matsuo, T. Omata, M. Yoshimura, J. Alloys Compd. 376 (2004) 262–267.
[16] V. Štengl, S. Bakardjieva, N. Murafa, Mater. Chem. Phys. 114 (2009) 217–226.
[17] N. Aman, P.K. Satapathy, T. Mishra, M. Mahato, N.N. Das, Mater. Res. Bull. 47 (2012) 179–183.
[18] J. Xiao, T. Peng, R. Li, Z. Peng, J. Ch Yan, Solid State Chem. 179 (2006) 1161–1170.
[19] C. Guzmán, G. del Ángel, R. Gómez, F. Galindo Hernández, C. Ángeles Chavez, Catal. Today 166 (2011) 146–151.
[20] A.M.T. Silva, C.G. Silva, G. Dražić, J.L. Faria, Catal. Today 144 (2009) 13–18.
[21] J.D. Figueroa, T. Fout, S. Plasynski, H. McIllvrid, P.D. Srivastava, Intl. J. Greenhouse Gas Control 2 (2008) 9.
[22] T. Seki, Y. Kokubo, S. Ichikawa, T. Suzuki, Y. Kayaki, T. Ikariya, Chem. Commun. (2009) 349.
[23] G. Liu, N. Hoivik, K. Wangn, H. Jakobsen, Solar Energy Mater, Sol. Cells 105 (2012) 53–68.
[24] Y. Wang, B. Li, Ch. Zhang, L. Cui, S. Kang, X. Li, L. Zhou, Appl. Catal. B: Environmental 130–131 (2013) 277–284.
[25] L. Matějová, T. Cajthaml, Z. Matěj, O. Benada, P. Klusoň, O. Šolcová, J. Supercrit. Fluids 52 (2010) 215–221.
[26] L. Matějová, V. Valeš, R. Fajgar, Z. Matěj, V. Holý, O. Šolcová, J. Solid State Chem. 198 (2013) 485–495.
[27] S. Brunauer, P.H. Emmett, E. Teller, J. Am. Chem. Soc. 60 (1938) 309–319.
[28] S.J. Gregg, K.S.W. Sing, Adsorption. Surface Area and Porosity, Academic Press, New York, 1982.
[29] J.B. DeBoer, B.C. Lippens, B.G. Linsen, J.C.P. Broekhoff, A.V.D. Heuvel, J. ThJ. Osinga, Colloid Interface Sci. 21 (1966) 405–414.
[30] A. Lecloux, J.P. Pirard, J. Colloid Interface Sci. 70 (1979) 265–281.
[31] P. Schneider, Appl. Catal. A 129 (1995) 157–165.
[32] Advanced Data Processing–Sorptomatic 1990 Users-Manual and software, Porotec GmbH, Germany, 2000.
[33] E.P. Barret, L.G. Joyner, P.B. Halenda, J. Am. Chem. Soc. 73 (1951) 373–380.
[34] B.F. Roberts, J. Colloid Interface Sci. 23 (1967) 266–273.
[35] Z. Matěj, R. Kužel, L. Nichtová, Powder Diffr. 25 (2010) 125–131.
[36] Z. Matěj, R. Kužel, MStruct - program/library for MicroStructure analysis by powder diffraction.<http://www.xray.cz/mstruct/>, 2009 (04.05.13).
[37] L. Matějová, Z. Matěj, O. Šolcová, Micropor. Mesopor. Mater. 154 (2012) 187–195.
[38] J. Tauc, Amorphous and Liquid Semiconductors, Plenum Press, London, 1974.
[39] K. Kočí, L. Obalová, L. Matějová, D. Plachá, Z. Lacný, J. Jirkovský, O. Šolcová, Appl. Catal. B: Environ. 89 (2009) 494–502.
[40] M.M. Ballari, R. Brandi, O. Alfano, A. Cassano, Chem. Eng. J. 136 (2008) 50–65.
[41] M.M. Ballari, R. Brandi, O. Alfano, A. Cassano, Chem. Eng. J. 136 (2008) 242–255.
[42] K. Kočí, L. Obalová, D. Plachá, Z. Lacný, Coll. Czech. Chem. Commun. 73 (2008) 1192–1204.
[43] J. Lin, J.C. Yu, J. Photochem. Photobiol. A 116 (1998) 63.
[44] J. Fang, X. Bi, D. Si, Z. Jiang, W. Huang, Appl. Surf. Sci. 253 (2007) 8952–8961.
[45] P. Scardi, M. Leoni, Acta Crystallogr. A 58 (2002) 190–200.
[46] T. López, F. Rojas, R. Alexander-Katz, F. Galindo, A. Balankin, A. Buljan, J. Solid State Chem. 177 (2004) 1873–1885.
[47] T. Ohsaka, F. Izumi, Y.J. Fujiki, Raman Spectrosc. 7 (1978) 321–324.
[48] W.H. Weber, K.C. Hass, J.R. McBride, Phys. Rev. B 48 (1993) 178–185.
[49] G. Li, D. Zhang, J.C. Yu, Phys. Chem. Chem. Phys. 11 (2009) 3775–3782.
[50] X. Gao, Y. Jiang, Y. Zhong, Z. Luo, K. Cen, J. Hazard. Mater. 174 (2010) 734–739.
[51] J. Zhu, J. Yang, Z.F. Bian, J. Ren, Y.M. Liu, Y. Cao, H.X. Li, H.Y. He, K.N. Fan, Appl. Catal. B: Environ. 76 (2007) 82–91.
[52] P. Burroughs, A. Hamnett, A.F. Orchard, G. Thornton, J. Chem. Soc., Dalton Trans. 17 (1976) 1686–1698.
[53] A. Kotani, T. Jo, J.C. Parlebas, Adv. Phys. 37 (1988) 37.
[54] G. Praline, B.E. Koel, R.L. Hance, H.I. Lee, J.M. White, J. Electron Spectrosc. Relat. Phenom. 21 (1980) 17–30.
[55] A. Pfau, K.D. Scheirbaum, Surf. Sci. 321 (1994) 71–80.
[56] E. Peparazzo, G.M. Ingo, N. Zacchetti, J. Vac. Sci. Technol. A 9 (1991) 1416–1420.
[57] N. Ozer, Sol. Energy Mater. Sol. Cells 68 (2001) 391–400.

[58] G. Magesh, B. Viswanathan, R.P. Viswanath, T.K. Varadarajan, Indian J. Chem. 48A (2009) 480–488.
[59] Y. Jiang, N. Bahlawane, J. Alloys Compd. 485 (2009) L52–L55.
[60] Y. Xu, Z. Zeng, J. Mol. Catal. A: Chem. 279 (2008) 77–81.
[61] F.B. Li, X.Z. Li, M.F. Hou, K.W. Cheah, W.C.H. Choy, Appl. Catal. A: Gen. 285 (2005) 181–189.

[62] L. Matějová, K. Kočí, M. Reli, L. Čapek, V. Matějka, O. Šolcová, L. Obalová, Appl. Surf. Sci. 285P (2013) 688–696.
[63] Y. Xu, H. Chen, Z. Zeng, B. Lei, Appl. Surf. Sci. 252 (2006) 8565–8570.
[64] F.B. Li, X.Z. Li, M.F. Hou, K.W. Cheah, W.C.H. Choy, Appl. Catal. A 285 (2005) 181–189.
[65] Y. Xie, C. Yuan, X. Li, Mater. Sci. Eng. B 117 (2005) 325–333.